

# Geophysical Research Letters

## RESEARCH LETTER

10.1029/2020GL090935

### Key Points:

- The Yutu-2 rover has been exploring along the rim of Finsen's secondaries, and pre-Finsen materials dominate the subsurface
- Crater density comparisons reveal that Orientale is a major source of the post-mare ejecta, explaining the radargram obtained
- Surface regolith detected by Yutu-2 is dominated by lower-crust materials ejected by Orientale, not related with SPA

### Supporting Information:

- Supporting Information S1

### Correspondence to:

Z. Xiao,  
[xiaozhiyong@mail.sysu.edu.cn](mailto:xiaozhiyong@mail.sysu.edu.cn)





### Citation:

Xiao, Z., Ding, C., Xie, M., Cai, Y., Cui, J., Zhang, K., & Wang, J. (2021). Ejecta from the Orientale basin at the Chang'E-4 landing site. *Geophysical Research Letters*, 48, e2020GL090935. <https://doi.org/10.1029/2020GL090935>

Received 23 SEP 2020

Accepted 28 NOV 2020

## Ejecta From the Orientale Basin at the Chang'E-4 Landing Site

Zhiyong Xiao<sup>1,2</sup> , Chunyu Ding<sup>1,3</sup> , Minggang Xie<sup>4</sup> , Yuzhen Cai<sup>1</sup> , Jun Cui<sup>1,2,5</sup> , Ke Zhang<sup>6</sup>, and Juntao Wang<sup>6</sup> 

<sup>1</sup>Planetary Environmental and Astrobiological Research Laboratory, School of Atmospheric Sciences, Sun Yat-sen University, Zhuhai, China, <sup>2</sup>Center for Excellence in Comparative Planetology, Chinese Academy of Science, Hefei, China, <sup>3</sup>Department of Earth and Space Sciences, Southern University of Science and Technology, Shenzhen, China, <sup>4</sup>College of Science, Guilin University of Technology, Guilin, China, <sup>5</sup>Key Laboratory of Lunar and Deep Space Exploration, National Astronomical Observatories, Chinese Academy of Sciences, Beijing, China, <sup>6</sup>Institute of Geochemistry, Chinese Academy of Sciences, Guiyang, China

**Abstract** Radargrams obtained by the Yutu-2 rover reveal that the post-mare deposits at the Chang'E-4 landing site are ~45 m thick, consistent with estimations based on orbital observations. Besides obvious ejecta from Finsen, polarized interpretations exist on whether or not the Alder crater is another contributor to the post-mare deposits, although predicted thicknesses of ejecta from all potential source craters are not adequately large compared to observations. We recognize that the rover has been exploring along a shared crater wall of two secondaries from Finsen. Mechanics of secondary impacts suggests that the discontinuous layers of coarse and fine materials observed in the radargram are older than Finsen. Cross-cutting relationships and crater density comparisons show that Alder is older than the mare basalts, and the Orientale basin was the major source for the post-mare materials. Lower-crust materials excavated by Orientale constituted a substantial portion of the surface regolith detected by the rover.

**Plain Language Summary** Understanding surface processes at the lunar farside and revealing potential compositions related with SPA are two scientific targets of the Chang'E-4 mission. Orbital observations and radargrams obtained by the rover show that the mare basalts at the landing area are covered by > 30 m thick deposits. Finsen has delivered bright rays to this area, but whether or not Alder is another source has been debated. Considering all potential sources that even include Alder, predicted thickness of post-mare materials is substantially less than observations. We recognize that Yutu-2 is exploring along the shared wall of two secondaries from Finsen, and subsurface materials are older than Finsen. Orientale's secondaries are traceable on top of Alder. The crater density on Orientale's ejecta deposits is comparable with that of the mare surface at the landing site, and morphological comparison of secondaries indicates that substantial ejecta had been deposited in Von Kármán before the volcanism in Leibnitz was ceased. The limited time window suggests that Orientale's ejecta were the only suitable source for the post-mare materials, forming the discontinuous layers of coarse and fine materials revealed in radargrams. Surface regolith examined by Yutu-2 should contain lower-crust materials that were excavated by Orientale.

## 1. Introduction

As the first successful surface exploration mission at the lunar farside, the Chang'E-4 lander and the Yutu-2 rover (Wu et al., 2019) have been exploring the lunar South Pole-Aitken basin (i.e., SPA). Together with the other sophisticated scientific payloads (Jia et al., 2018), the lunar penetrating radar (i.e., LPR) and the visible-near-infrared spectrometer (i.e., VNIS) onboard the rover are returning invaluable data on subsurface structures and surface compositions, aiming at understanding both surface processes at the lunar farside and possible compositions related with SPA. Interpretations of planetary remote sensing data usually face nonuniqueness (Baker, 2015). Likewise, data obtained by both the LPR and VNIS have already yielded diverged geological interpretations. For example, based on VNIS reflectance spectra for surface regolith, it is debated whether or not substantial olivine could be indicated (Gou et al., 2019, 2020; Huang et al., 2020; Li et al., 2019; Lin et al., 2019); LPR radargrams revealed layered structures in the subsurface, and inconsistent interpretations exist about their origins (Lai et al., 2020, 2019; Li et al., 2020; Zhang et al., 2020). Regional

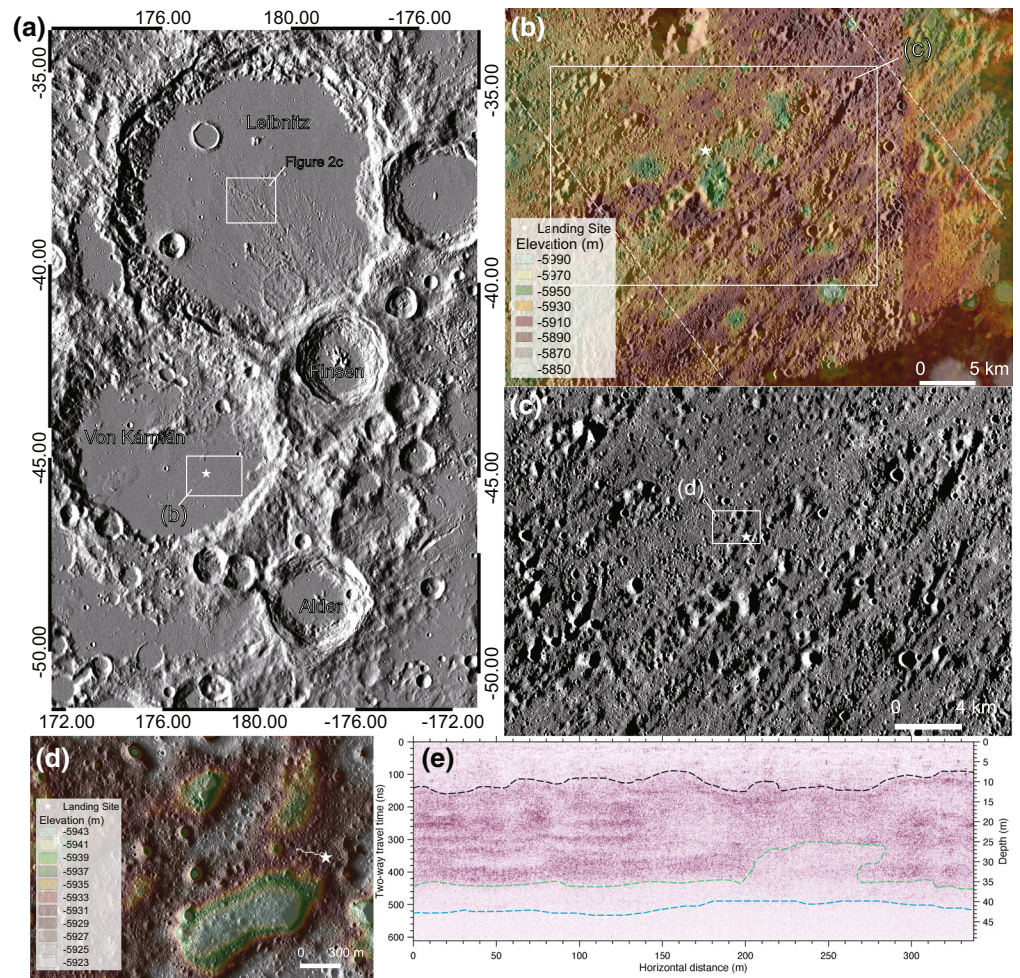


**Figure 1.** Regional and local context of the Chang'E-4 landing site (white stars). (a) The landing site is located on a mare unit in the floor of Von Kármán. The canvas uses the shade relief map based on the LOLA global DTM. (b) Lineations sourced from Finsen dominate the regional topography. The two white dashed lines mark the high topography area on the mare reported by Di et al. (2019). The base image is a Kaguya TC mosaic that is overlain by a Selene-LOLA DTM (SLDEM; Barker et al., 2016). (c) The landing site is located within a chain of secondaries, which is ~140 km to the center of Finsen (Kaguya TC). (d) The route of Yutu-2 in the first 12 lunar days (white curve) was located on a shared wall of two secondaries from Finsen. The base image is LROC NAC\_DTM\_CHANGE4\_E458S1775 overlying LROC NAC M178833263L. (e) Radargrams obtained by the high-frequency LPR in the first 12 lunar days. The warm and cold colors are relative strengths of echoes. The black curve denotes the boundary between surface fine materials and deeper coarse materials, the green curve denotes the bottom of the coarse materials, and echo strengths are undifferentiated from noises at the blue curve. The strength and spatial distribution of echoes are referred to the subjective assignment of the boundaries.

context is the framework for the interpretation of remote sensing data, and the emerged debates are largely caused by incomplete understanding of the geological history of the landing area.

The landing site is located on a mare surface, which has been covered by younger impact ejecta from various sources. Geological mapping based on crosscutting relationships (Fortezzo et al., 2020; Yingst et al., 2017) and age determination based on crater counts (Haruyama et al., 2009; Huang et al., 2018; Ling et al., 2019; Pasckert et al., 2018) both suggested a lower-Imbrian age for the mare basalts, formed around 3.6–3.7 billion years ago. Bright impact rays and secondaries formed by the Eratosthenian-aged Finsen crater are pronounced in the landing area (Huang et al., 2018), and abundant secondaries younger than Finsen are also visible (Figure 1). Based on small craters that have and have not excavated mare basalts, the post-mare debris is estimated to be mostly >34 m thick (Huang et al., 2018; Li et al., 2020; Ling et al., 2019). This

estimation is consistent with the depth distribution of echo patterns in LPR radargrams, as the first sharp transition from weak to strong echoes, which was interpreted as the boundary between the younger debris cover and deeper competent mare basalts, is located at ~45 m (Lai et al., 2020; Zhang et al., 2020).

Insufficient local context has led to disagreements about the possible provenance of post-mare deposits. A persistent debate is the relative age between the Alder crater and the mare unit in the landing area (Figure 1a). Geological mapping (Fortezzo et al., 2020; Yingst et al., 2017) and recent crater statistics (Lu et al., 2020) suggested that Alder is older. Based on a belt of raised topography on the mare unit (Figure 1b), one interpretation argued that Alder was younger (Di et al., 2019), although topographic bumps on lunar mare that are not related with impact ejecta are common. On the other hand, referring to reported stratigraphic ages of impact craters, a ballistic sedimentation model that has considered both primary ejecta deposition and excavation of local materials by secondary impacts (Xie, Liu et al., 2020) was employed to estimate the thickness of ejecta delivered by various post-mare craters around the landing site (Huang et al., 2018; Lai et al., 2020). For craters that are stratigraphically younger than the mare basalts, only a few were capable to deliver nonnegligible ejecta (>0.2 m) to the landing area, considering that ejecta thickness decreases exponentially away from the parent crater (Huang et al., 2018; Lai et al., 2020). The estimated total thickness of primary ejecta from all known source craters is less than 10 m (Huang et al., 2018). Even assuming Alder had delivered impact ejecta to the mare surface (~8 m thick; Lai et al., 2020), the estimated total thickness of primary ejecta plus local excavation is much less than the observed thickness of post-mare deposits. Nevertheless, Alder has been frequently cited as a post-mare crater to explain the thick debris cover (e.g., Zhang et al., 2020).

Sorting out the post-mare stratigraphy is critically important to interpret the scientific data returned. Reflectance spectra obtained from orbit showed that at pixel scales of ~100–200 m, surface regolith in the landing area is generally non-basaltic in composition (Huang et al., 2018; Ling et al., 2019). It has been a consensus that ejecta from Finsen are the major source of the surface regolith (Li et al., 2019; Gou et al., 2020; Huang et al., 2020; Lin et al., 2019). However, ballistic sedimentation models predicted a dominance of mare basalts in the debris cover that was excavated by distal ejecta (Lai et al., 2020). Essentially, lunar regolith is a weathering product (McKay et al., 1991). LPR radargrams (Figure 1e) showed that the top ~10–13 m thick materials have similar dielectric properties with typical lunar regolith (Ding et al., 2020; Lai et al., 2019; Li et al., 2020). This thickness is much larger than that on similar-aged lunar mare, requiring unusually fast growth for the entire regolith column at the landing site (Lai et al., 2019). For comparison, the predicted thickness of Finsen's ejecta and their local excavation was <8 m at the landing site (Huang et al., 2018; Lai et al., 2020), which is contradicted with the top ~10–13 m thick materials being entirely developed in Finsen's ejecta (Lai et al., 2019). One hydrocode simulation argued that Finsen's ejecta were >30 m thick at the landing site (Di et al., 2019), which was not supported by observations based on reflectance spectra (Li et al., 2020; Qiao et al., 2019) or predictions based on ballistic sedimentation models (Huang et al., 2018; Lai et al., 2020). On the other hand, discontinuous layering of weak and strong echoes are observed in the LPR radargrams (Figure 1e), with the consensus being emplaced as distal ejecta (Lai et al., 2020, 2019; Li et al., 2020; Zhang et al., 2020). However, emplacement of distal ejecta does not occur via simple carpeting. Observations of various populations of secondary craters suggested that excavation of local materials and simultaneous resurfacing by ejecta delivered from uprange secondaries are vitally important (Xiao, 2016, 2018). Therefore, the formation of the layered echoes in the radargram (Figure 1e) needs an explanation in the frame of ejecta deposition.

Here we provide a new perspective on the geologic context of the Chang'E-4 landing site. We notice that while Finsen's ejecta indeed have dominated the landing area, locally, both the landing site and rover route are located on top of a shared crater wall of two secondaries formed by Finsen. Mechanics of secondary impacts suggests that the subsurface materials are older than Finsen (Section 3.1). Analyses of LPR radargram confirm that competent mare basalts occur at depths larger than ~45 m (Section 3.2). Based on crater density comparisons, we independently verify that Alder is older than the mare basalts and further show that the Orientale basin is an unnoticed major source (Section 3.3). The emplacement mechanism of basin ejecta is investigated to explain the alternatively strong and weak echoes in the radargram (Section 4.1). With a reconstructed local stratigraphy, interpretation of compositional data obtained by the rover is reoriented (Section 4.2).



## 2. Data and Methods

The morphology and geometry of the landing area are studied at different scales using data obtained by the Narrow Angle Camera (NAC) and Wide Angle Camera (WAC) of the Lunar Reconnaissance Orbiter Camera (LROC; Robinson et al., 2010), the Terrain Camera (TC; Haruyama et al., 2008) onboard the Kaguya mission, and the Lunar Orbiter Laser Altimeter (LOLA; Smith et al., 2010). The IDs and sources of imagery and topography data used in this study are summarized in Table S1.

Crater densities are used to represent relative ages to identify additional sources of post-mare deposits besides Finsen. The cease of mare volcanism in Von Kármán occurred >1 billion years before the formation of the Finsen crater, and numerous impacts have occurred on the Moon during this time (Huang et al., 2018; Lu et al., 2020). Previous studies screened possible source craters based on their stratigraphic ages and distances to the landing area, and major ejecta suppliers such as the Leibnitz crater and the Ingenii and Imbrium basins were safely ruled out (Huang et al., 2018; Ling et al., 2019; Lai et al., 2020). Except for the debated Alder crater, no other pre-Finsen craters were identified that might have contributed nonnegligible ejecta to the post-mare deposits (Huang et al., 2018; Lai et al., 2020). Meanwhile, discrepancies between stratigraphic ages and absolute model ages derived from crater counts have been widely noticed for given craters (Xie, Xiao et al., 2020). Instead of globally cataloging absolute model ages for impact craters using crater statistics, this study uses the candidate early Imbrian source craters that were reported to be slightly older than the mare basalts at the landing area (Lai et al., 2020). For the mare surface at the landing site, the spatial densities of craters larger than 1 and 2 km in diameters,  $N(1)$  and  $N(2)$  respectively, are referred from Huang et al. (2018), Pasckert et al. (2018), and Ling et al. (2019). The Orientale Basin has caused voluminous melting and delivered widespread light plains across the Moon (Meyer et al., 2016), and their  $N(1)$  values were referred as the crater density of Orientale. Lu et al. (2020) reported model ages of ~3.5 and 3.2–3.3 Ga for Alder and the landing mare, respectively. The results are substantially less than both their stratigraphic ages (Yingst et al., 2017) and results from other crater statistics (Huang et al., 2018; Ling et al., 2019; Pasckert et al., 2018). To provide an independent evaluation, several areas on both the continuous ejecta deposits and floor of the Alder crater were selected as counting areas (Figure S1). For the completeness of crater collection and avoiding possible contamination by secondaries, only craters larger than 10 pixels of the base images were used (Wang et al., 2020). Table S2 in the appendices enumerates the crater densities compared. All the  $N(1)$  and  $N(2)$  values compared are derived directly from crater counts instead of being fitted from smaller craters using a production function.

Radargrams obtained by the high-frequency lunar penetrating radar (Fang et al., 2014) were used to study the internal structures of the post-mare deposits. The rover has traveled over 500 m by September 2020. For the purpose of this study, data obtained in the first 12 lunar days (until January 1, 2020) are adequate (~340 m). Processing of the LPR data includes the following steps: removal of redundant data, dewow filtering, amplitude compensation, background subtraction, and band-pass filtering. To facilitate geological interpretation of the radargram, migration transformation was performed to highlight echo contrasts (Figure 1e). In the supplementary information, Text S1 shows the detailed processing procedure, and Figures S2–S7 are the intermediate results.

## 3. Results

### 3.1. New Perspective on the Local Context

The topography of the landing area is mainly shaped by the northeast-to-southwest trending lineations (Figure 1), which are remnant topography of chains of secondaries formed by Finsen (Huang et al., 2018). The landing site is located within such a chain (Figures 1b and 1c), which exhibits similar morphology and strike with the other secondaries of Finsen (Figure 1c). Low-sun images with sub-meter pixel scales show that both the landing site and rover path are located on an east-to-west trending ridge (Figure 1d). The ridge is the shared wall of two heavily degraded secondaries in the chain (Figure 1c). The two secondaries have rim-to-rim lengths of >1 km and widths of ~700 m, and the landing site is ~6 and 20 m above the floors of the two secondaries, respectively (Figure 1d). Topography degradation has substantially reduced

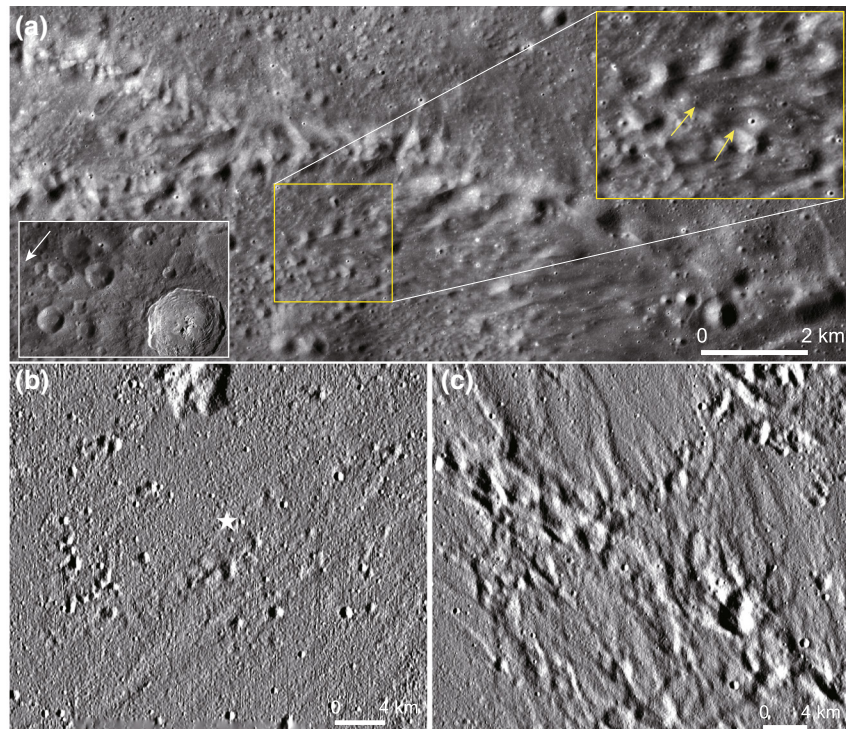


**Figure 2.** Formation and degradation of lunar secondaries. (a) Secondaries of the Jackson crater are resurfaced by flow-like materials that are ejecta delivered by secondary impacts at the uprange portion of this chain. Herringbone patterns are constructed by the flows, and yellow arrows in the inset point to layers in the flow. Jackson has a similar diameter with Finsen, and both the sizes and ballistic ranges of secondaries shown here are comparable with those at the Chang'E-4 landing site (Figure 1d). The white arrow in the lower-left inset shows the location of the main figure. (b) Finsen's secondaries on the mare unit in Von Kármán are much more degraded than those on the slightly younger mare unit in Leibnitz (c). The white star denotes the landing site. The base image of (a) is from Kaguya TC, and that of (b) and (c) is shade relief map constructed from SLDEM.

the original rim heights, broadening the rim width, and the current depth-to-diameter ratios are  $<0.02$  and local slopes are  $<2^\circ$  (Figure S8).

Materials beneath the rover route are older than Finsen. Crater walls are structurally deformed target materials that are subsequently exposed by the collapse of transient cavities, and excavated target materials are deposited on crater rims (Melosh, 1989). Therefore, walls of secondaries consist of pre-impact target, and Finsen's ejecta that have formed the secondaries shown in Figure 1d were distributed outside of the chain. Irregularly shaped secondaries in chains and clusters are most likely formed by a cluster of primary ejecta, instead of a single fragment (Schultz & Gault, 1985). Depending on the spatial dispersion of primary ejecta, secondaries in a chain exhibit various morphology and geometry (Xiao, 2016), so the initial geometry of the two secondaries shown in Figure 1d was unpredictable. On the other hand, for a chain of secondaries, materials exhibiting flow characteristics are commonly visible across secondaries in the downrange direction, which are ejecta launched by secondary impacts in the uprange direction of the chain (Luchhitta, 1977; Xiao, 2016). Figure 2a shows the morphology of such flows across secondaries that are  $\sim 140$  km to the center the Jackson crater, which has a similar rim-to-rim diameter ( $D = \sim 71$  km) with Finsen. Self-destruction among secondaries by immediately followed sweeping flows occurs in a spatially discontinuous manner (Xiao, 2016), and layering of flow deposits is usually observed (Figure 2a). Cratering mechanics suggests that most ejecta launched by subsonic secondary impacts are local target materials, instead of shattered primary ejecta that formed the secondaries (Schultz & Gault, 1985). As the original geometry of secondaries and local thickness of subsequent flows cannot be constrained, initial stratigraphic column of the two secondaries cannot be quantitatively constrained. Nevertheless, the post-degradation walls of secondaries, at least for the remnant height of  $\sim 20$  m (Figure 1d), are dominated by pre-Finsen materials.

### 3.2. Relative Permittivity of Pre-finsen Materials

The high-frequency LPR is capable to resolve materials down to  $\sim 520$  nm before echo strengths are differentiated from noises (Figure S9). In radargrams obtained by the low-frequency LPR, the debris cover on top of the integrated mare basalts occurs as a weak and more or less a homogenous unit ( $\sim 600$  ns), and deeper materials exhibit much stronger echoes (Lai et al., 2020; Zhang et al., 2020). The high-frequency LPR features higher spatial resolutions (Fang et al., 2014), and three major units with different relative echo strengths are recognized in the debris cover (Figure 1e). The first unit, including the surface regolith, exhibits relatively homogenous and weak echoes (Figure 1e), indicating a similar bulk permittivity with that of typical regolith (Ding et al., 2020; Lai et al., 2020, 2019; Li et al., 2020). The second unit is composed of discontinuous and uneven stacks of strong and weak echoes (Li et al., 2020), and the contacts are transitional instead of abrupt (Figure 1e). Relative permittivity of lunar materials is mainly affected by the bulk density (Carrier et al., 1991), so compared to the first unit, the second unit is mainly composed of relative dense materials, with pockets of more porous materials are interbedded. Deeper echoes are similarly weak as the first unit, and a slightly strong horizon is visible at  $\sim 510$  ns before noises dominating the signal (Figure 1e).

Geometry of hyperbolic echo patterns in the radargram is employed to estimate the relative permittivity of subsurface materials (see supplementary text for method; Daniels, 1989), so the two-way travel times can be translated to depths (Figure 1e). Twelve reflectors that have integrated hyperbolic shapes are recognized in the first 20–230 ns of the radargram, and the Figure S10 shows their morphology. The reflectors are caused by materials with a higher relative permittivity than the surrounding, which are normally formed by competent boulders. The derived relative permittivities are  $\sim 2.6$ – $4.3$ , with an average value is  $\sim 3.4$  (Table S3). Therefore, materials within the equivalent depths of 230 ns ( $\sim 18$  m) have similar bulk densities with typical lunar regolith (Figure S11; Carrier et al., 1991), concurring the overall weak echoes detected by the low-frequency LPR (Lai et al., 2020; Zhang et al., 2020). Although materials deeper than  $\sim 10$  m exhibit relatively strong echoes (Figure 1e), the entire second unit follows an overall similar echo pattern, suggesting that materials at  $\sim 10$ – $37$  m are coarse debris instead of competent rocks. In conclusion, we support that integrated mare basalts that were not substantially disturbed by ejecta deposition occur at depths  $> \sim 45$  m (Zhang et al., 2020), and the debris cover is composed by layers of coarse and fine particles.

### 3.3. Orientale as a Dominate Source of Pre-Finsen Ejecta

The  $\sim 45$  m thick post-mare deposits are dominated by distal ejecta from pre-Finsen craters and excavated local basalts are minor, since the surface materials are generally non-basaltic in composition (Huang et al., 2018). Finsen's secondaries at the landing area (Figure 2b) are more degraded than those with similar ballistic ranges on the floor of Leibnitz (Figure 2c). This sharp contrast indicates that before Finsen was formed, the mare unit in Von Kármán had been covered by thicker porous materials than that in Leibnitz, so both the initiation of ejecta flows by secondary impacts and post-impact degradation by mass wasting were enhanced in Von Kármán. As predicted by lunar crater chronology, the mare volcanism in Leibnitz occurred only  $\sim 380$  million years later than that in Von Kármán (Pasckert et al., 2018). Therefore, before the cease of mare volcanism in Leibnitz, a limited number of craters were able to deliver a significant amount of ejecta to the landing area.

Unlike the obvious secondaries formed by Finsen (Figure 1), older craters have not left topographic evidence at the landing site. Crater populations collected on both the floor and different ejecta facies of Alder uniformly exhibit a much larger density in terms of both  $N(1)$  and  $N(2)$  values than the mare basalts in Von Kármán (Table S2). This result verifies both geological maps that assigned a Pre-Imbrian age for Alder (Fortezzo et al., 2020) and the other crater density comparisons (Lu et al., 2020). On the other hand, crater densities on Orientale's light plains (Meyer et al., 2016) are comparable with that on the mare unit in Von Kármán (Huang et al., 2018; Ling et al., 2019; Pasckert et al., 2018), which are further verified by their overlapped model ages ( $\sim 3.7$  Ga) as predicted using the same crater chronology system (Ling et al., 2019; Whitten et al., 2011). In conclusion, Alder is much older than the mare basalts in Von Kármán, and the Orientale basin is a suitable candidate that has delivered ejecta to the landing site.



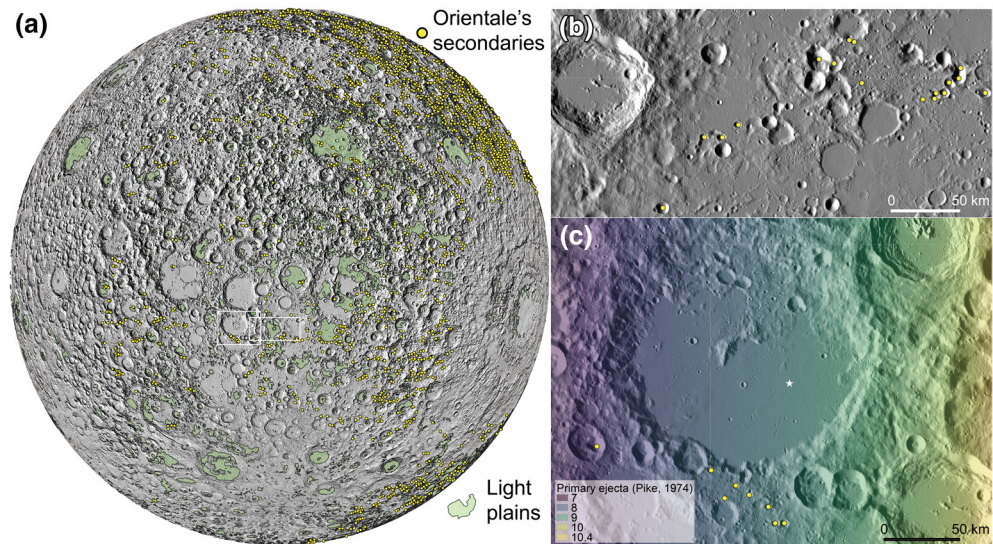


**Figure 3.** Existence of Orientale deposits at the Chang'E-4 landing site. (a) Spatial distributions of Orientale's secondaries (yellow dots; Guo et al., 2018) and global distribution of light plains (Meyer et al., 2018) at the lunar farside. Not all the light plains were formed by Orientale. The canvas is the shade relief map constructed based on the LOLA global DTM, and the Orientale basin is located at the right edge. (b) Orientale's secondaries (yellow dots) are traceable on top of Finsen's ejecta. (c) Orientale's ejecta at the landing area (white star) are  $\sim 8$  m thick as predicted by Pike (1974), but Orientale's secondaries nearby are as large as  $\sim 7$  km (yellow dots), representing up to hundreds of meters of primary ejecta. Panels (b) and (c) are based on SLDEM shade relief maps, and the location is marked in panel (a).

As a first-order estimation, ballistic sedimentation model (Pike, 1974; Xie, Liu et al., 2020) predicted that the Orientale basin has delivered  $>8$  m thick primary ejecta to the landing site (Figure 3), and their local excavated materials are  $\sim 118$  m thick (Lai et al., 2020). Together with the crater density comparison (Table S2), this estimation suggests that ejecta delivered by the Orientale basin cannot be ignored as a major component of the post-mare deposits. However, the actual thickness of primary ejecta and their local excavation can deviate substantially from predictions, as ballistic sedimentation models are based on simplified assumptions, such as azimuthally symmetric ejecta deposition, similar cratering scaling laws for secondary and primary impacts, and ignorance of downrange flows triggered by secondaries. Orientale's secondaries as large as  $\sim 10$  km are visible around the Von Kármán crater, and some are superposed on the ejecta deposits of Alder (Figure 3), further proving that Alder is older than Orientale. Primary ejecta that formed such secondaries had equivalent dimensions of  $>500$  m (Guo et al., 2018), which are comparable with the thickness of light plains formed by Orientale (Meyer et al., 2016). The co-occurrence of light plains and secondaries formed by Orientale (Figure 3a) suggests that with identical ballistic ranges, deposition of distal ejecta can be substantially different, although the detailed mechanism awaits further investigations. Compared to the other potential lower-Imbrian aged source craters (Lai et al., 2020), Orientale is the only candidate that is capable of accounting for a substantial, if not most of the post-mare deposits at the landing site.

## 4. Discussion

### 4.1. Sandwich Structures in Orientale's Distal Ejecta

Orientale being the dominate source of the post-mare deposits is consistent with a thicker debris cover on the mare basalts in Von Kármán before volcanism was stopped in Leibnitz (Section 3.3). This interpretation further corroborates observations by the low-frequency LPR that the top  $\sim 45$  m materials are composed by more porous materials than competent basalts (Zhang et al., 2020), since Orientale's distal ejecta should be porous breccias (Cai et al., 2020). The interpretation also explains the much larger regolith thickness at the landing site than same-aged lunar mare (Lai et al., 2019), as the starting materials for regolith development were already porous breccia instead of competent rocks. Besides these concordances, the actual thickness of

both Orientale's ejecta and their locally excavated materials is *sensu stricto* not precisely known, since both ejecta thickness and their emplacement mechanism are spatially heterogeneous (Figure 3c).

The second unit shown in Figure 1e was interpreted as layers of ejecta delivered by different but unknown source craters older than Finsen (Li et al., 2020; Lai et al., 2020; Zhang et al., 2020). We provide an alternative interpretation that links the origin of the second unit to the emplacement of Orientale's ejecta (Figure 3e). Ejecta emplacement is a highly dynamical process. The different landing times of individual ejecta fragments in a swarm and their residual momentum would cause horizontal shearing within the deposits (Figure 2a; Hörz et al., 1983). Layers of fluidized materials have also been observed feeding the light plains formed by Orientale (Meyer et al., 2016). Seismic reflections in the upper 220 meters of the Cayley Plains at the Apollo 16 landing site also feature alternative weak and strong echoes, which were formed by Imbrium's ejecta (Cooper et al., 1974). Therefore, the stacks of relative dense materials and lens of more porous materials in the second unit of the radargram (Figure 3e) may be breccias that have different bulk densities emplaced by Orientale's distal ejecta. This interpretation is also applicable for both the first and third units (Figure 1e), if assuming that the entire ~45 m post-mare deposits were emplaced by Orientale.

#### 4.2. Ancient Highland Crust Detected by the Yutu-2 Rover

The new perspective that Orientale's ejecta being the dominate source of the post-mare deposits completely changes provenance interpretations for the surface regolith at the landing site. VNIS cannot unambiguously differentiate plagioclase, because plagioclase exhibits rather weak absorption features in VNIS wavelengths of 450–2,395 nm, which are easily masked by a minor presence of other mafic minerals (Cheek & Pieters, 2014). Using different algorithm parameters to estimate mineral components based on VNIS data, the interpreted mineralogy was sharply different, such as the possible percentage of olivine (Li et al., 2019; Gou et al., 2019; Lin et al., 2019). For the deconvolution of VNIS data, one critical parameter in the center of discussion is whether or not plagioclase and other phases were adequately considered as end members (Huang et al., 2020). Current interpretations favor that both the surface regolith and some rock fragments measured by VNIS are noritic that is rich in plagioclase and pyroxene (Huang et al., 2020). We argued that Orientale's ejecta is the major source of the surface regolith, which should be ancient highland crustal materials, since Orientale did not excavate mantle materials as predicted by numerical modeling (Johnson et al., 2016; Potter et al., 2013). The noritic composition of surface regolith further indicates that Orientale's ejecta at the landing site were mainly from the lower crust of the Moon, largely unrelated with SPA.

### 5. Conclusion

There are many interpretations of the surface compositional and subsurface structures at the Chang'E-4 landing site, but it has been a consensus that Finsen's ejecta are the dominate source for the surface regolith, while older craters that might have contributed ejecta to the post-mare deposits are not known. We reveal that both the landing site and the rover route are located on a shared wall of two heavily degraded secondaries from Finsen (Figure 1d), so that local materials are older. Different preservation states of Finsen's secondaries suggest that during the short hiatus of mare vocalism in Von Kármán and Leibnitz, substantial ejecta were deposited at the landing area. Crater density comparisons and overlapping relationships preclude Alder and verify Orientale as the dominate source. This recognition provides a sententious explanation for the missed source craters, origin of layered interior structures in radargrams, cause of the thicker-than-normal local regolith, and reason of different preservation states of Finsen's secondaries. We appeal for a re-evaluation on interpretations of compositional data obtained by the rover, since the subsurface materials may be lower-crust materials excavated by the Orientale basin.

#### Data Availability Statement

Imagery and topography data obtained by lunar orbiters are available in the NASA Planetary Data System archive (<https://pds-geosciences.wustl.edu>), and Table S1 shows the IDs and available addresses for the data. The authors thank the two reviewers for the constructive comments and suggestions. Z. Xiao



conceived the research, designed the analyses, performed the observation, and wrote the manuscript. C. Ding analyzed the LPR data, Y. Cai and M. Xie helped estimated eject thickness. All authors contributed to discussions and writing.

**Acknowledgment**

The Chang'E-4 mission was carried out by the Chinese Lunar Exploration Program, and the scientific data are provided by China National Space Administration. The authors are supported by the B-type Strategic Priority Program of the Chinese Academy of Sciences [grant number XDB41000000], the National Natural Science Foundation of China [grant number 41773063, 42004099, 41941003, 41773065, and 41490634], the Pre-research Project on Civil Aerospace Technologies of China National Space Administration [grant number D020101 and D020202], the Science and Technology Development Fund of Macau [grant number 0042/2018/A2], the Chinese Academy of Sciences Interdisciplinary Innovation Team, and the Key Program of Frontier Science of Chinese Academy of Sciences (Grant QYZDY-SSW-DQC028).

**References**

Baker, V. R. (2015). Planetary geomorphology: Some historical/analytical perspectives. *Geomorphology*, *250*, 8–17.

Barker, M. K., Mazarico, E., Neumann, G. A., Zuber, M. T., Haruyama, J., & Smith, D. E. (2016). A new lunar digital elevation model from the lunar orbiter laser altimeter and SELENE terrain camera. *Icarus*, *273*, 346–355. <https://doi.org/10.1016/j.icarus.2015.07.039>

Cai, Y., Xiao, Z., Ding, C., & Cui, J. (2020). Fine debris flows formed by the Orientale Basin. *Earth and Planetary Physics*, *4*, 212–222.

Carrier, W. D., Olhoeft, G. R., & Mendell, W. (1991). Physical properties of the lunar surface. In G. H. Heiken, D. T. Vaniman, & B. M. French (Eds.), *Lunar sourcebook: A user's guide to the Moon* (pp. 285–356). Cambridge: Cambridge University Press.

Cheek, L. C., & Pieters, C. M. (2014). Reflectance spectroscopy of plagioclase-dominated mineral mixtures: implications for characterizing lunar anorthosites remotely. *American Mineralogist*, *99*(10), 1871–1892.

Cooper, M. R., Kovach, R. L., & Watkins, J. S. (1974). Lunar near-surface structure. *Reviews of Geophysics and Space Physics*, *12*, 291–308.

Daniels, J. J. (1989). *Fundamentals of ground penetrating radar*. Proceedings of the Symposium on the Application of Geophysics to Engineering an Environmental Problems (pp. 62–142). SAGEEP 89, Golden, Colorado.

Ding, C., Xiao, Z., Wu, B., Li, Y., Prieur, N. C., Cai, Y., et al. (2020). Fragments delivered by secondary craters at the Chang'e 4 landing site. *Geophysical Research Letters*, *47*, e2020GL087361. <https://doi.org/10.1029/2020GL087361>

Di, K., Zhu, M.-H., Yue, Z., Lin, Y., Wan, W., Liu, Z., et al. (2019). Topographic evolution of Von Kármán crater revealed by the lunar rover Yutu-2. *Geophysical Research Letters*, *46*, 12764–12770. <https://doi.org/10.1029/2019GL085252>

Fang, G., Zhou, B., Ji, Y., Zhang, Q., Shen, S., Li, Y., et al. (2014). Lunar penetrating radar onboard the Chang'e-3 mission. *Research in Astronomy and Astrophysics*, *14*(12), 1607–1622. <https://doi.org/10.1088/1674-4527/14/12/009>

Fortezzo, C. M., Spudis, P. D., & Harrel, S. L. (2020). *Release of the Digital Unified Global Geologic Map of the Moon At 1:5,000,000-Scale*. Paper presented at 51st Lunar and Planetary Science Conference, Lunar and Planetary Institute, Houston, TX. <https://www.hou.usra.edu/meetings/lpsc2020/pdf/2760.pdf>

Gou, S., Di, K., Yue, Z., Liu, Z., He, Z., Xu, R., et al. (2019). Lunar deep materials observed by Chang'e-4 rover. *Earth and Planetary Science Letters*, *528*, 115829. <https://doi.org/10.1016/j.epsl.2019.115829>

Gou, S., Di, K., Yue, Z., Liu, Z., He, Z., Xu, R., et al. (2020). Forsteritic olivine and magnesium-rich orthopyroxene materials measured by Chang'e-4 rover. *Icarus*, *345*, 113776. <https://doi.org/10.1016/j.icarus.2020.113776>

Guo, D., Liu, J., Head, J. W., III, & Kreslavsky, M. A. (2018). Lunar Orientale impact basin secondary craters: Spatial distribution, size-frequency distribution, and estimation of fragment size. *Journal of Geophysical Research: Plan*, *123*, 1344–1367. <https://doi.org/10.1029/2017JE005446>

Haruyama, J., Matsunaga, T., Ohtake, M., Morota, T., Honda, C., Yokota, Y., et al. (2008). Global lunar surface mapping experiment using the Lunar Imager/Spectrometer on SELENE. *Earth Planetary and Space*, *60*, 243–256.

Haruyama, J., Ohtake, M., Matsunaga, T., Morota, T., Honda, C., Yokota, Y., et al. (2009). Long-lived volcanism on the lunar farside revealed by SELENE Terrain Camera. *Science*, *323*(5916), 905–908. <https://doi.org/10.1126/science.1163382>

Hörz, F., Ostertag, R., & Rainey, D. A. (1983). Bunte Breccia of the Ries continuous deposits of large impact craters. *Reviews of Geophysics and Space Physics*, *21*, 1667–1725.

Huang, J., Xiao, Z., Flahaut, J., Martinot, M., Head, J., Xiao, X., et al. (2018). Geological characteristics of Von Kármán crater, north-western south pole-Aitken Basin: Chang'E-4 landing site region. *Journal of Geophysical Research: Plan*, *123*, 1684–1700. <https://doi.org/10.1029/2018JE005577>

Huang, J., Xiao, Z., Xiao, L., Horgan, B., Hu, X., Lucey, P., et al. (2020). Diverse rock types detected in the lunar South Pole–Aitken Basin by the Chang'E-4 lunar mission. *Geology*, *48*(7), 723–727. <https://doi.org/10.1130/G47280.1>

Jia, Y., Zou, Y., Ping, J., Xue, C., Yan, J., & Ning, Y. (2018). The scientific objectives and payloads of Chang'E-4 mission. *Planetary and Space Science*, *162*, 207–215.

Johnson, B. C., Blair, D. M., Collins, G. S., Melosh, H. J., Freed, A. M., Taylor, G. J., et al. (2016). Formation of the Orientale lunar multiring basin. *Science*, *354*, 441–444.

Lai, J., Xu, Y., Bugliacchi, R., Meng, X., Xiao, L., Xie, M., Liu, B., et al. (2020). First look by the Yutu-2 rover at the deep subsurface structure at the lunar farside. *Nature Communications*, *11*, 3426. <https://doi.org/10.1038/s41467-020-17262-w>

Lai, J., Xu, Y., Zhang, X., Xiao, L., Yan, Q., Meng, X., et al. (2019). Comparison of dielectric properties and structure of lunar regolith at Chang'e-3 and Chang'e-4 landing sites revealed by ground penetrating radar. *Geophysical Research Letters*, *46*, 12783–12793. <https://doi.org/10.1029/2019GL084458>

Li, C., Liu, D., Liu, B., Ren, X., Liu, J., He, Z., et al. (2019). Chang'e-4 initial spectroscopic identification of lunar far-side mantle-derived materials. *Nature*, *569*(7756), 378–382. <https://doi.org/10.1038/s41586-019-1189-0>

Li, C., Su, Y., Pettinelli, E., Xing, S., Ding, C., Liu, J., et al. (2020). The Moon's farside shallow subsurface structure unveiled by Chang'e-4 lunar penetrating radar. *Science Advances*, *6*(9), eaay6898. <https://doi.org/10.1126/sciadv.aay6898>

Ling, Z., Qiao, L., Liu, C., Cao, H., Bi, X., Lu, X., et al. (2019). Composition, mineralogy and chronology of mare basalts and non-mare materials in Von Kármán crater: Landing site of the Chang'e-4 mission. *Planetary and Space Science*, *179*(104), 741. <https://doi.org/10.1016/j.pss.2019.104741>

Lin, H., He, Z., Yang, W., Lin, Y., Xu, R., Zhang, C., et al. (2019). Olivine-norite rock detected by the lunar rover Yutu-2 likely crystallized from the SPA impact melt pool. *National Science Review*, *7*, 913–920. <https://doi.org/10.1093/nsr/nwz183>

Luchhitta, B. K. (1977). Crater clusters and light mantle at the Apollo 17 site: A result of secondary impact from Tycho. *Icarus*, *30*, 80–96.

Lu, Y., Wu, Y., Michael, G. G., Ma, J., Cai, W., & Qin, N. (2020). Chronological sequence of Chang'E-4 landing zone within Von Kármán crater. *Icarus*, *354*, 114086. <https://doi.org/10.1016/j.icarus.2020.114086>

McKay, D. S., Heiken, G., Basu, A., Blanford, G., Simon, S., Reedy, R., et al. (1991). The lunar regolith. In G. H. Heiken, D. T. Vaniman, & B. M. French (Eds.), *Lunar sourcebook: A user's guide to the Moon* (pp. 285–356). Cambridge: Cambridge University Press.

Melosh, H. J. (1989). *Impact Cratering: A Geologic Process*. New York, NY: Oxford Univ. Press.

Meyer, H. M., Denevi, B. W., Boyd, A. K., & Robinson, M. S. (2016). The distribution and origin of lunar light plains around Orientale basin. *Icarus*, *273*, 135–145. <https://doi.org/10.1016/j.icarus.2016.02.014>

- Meyer, H. M., Robinson, M. S., Denevi, B. W. & Boyd, A. K. (2018) *A new global map of light plains from the Lunar Reconnaissance Orbiter*. Paper presented at the 49th Lunar and Planetary Science Conference, Lunar and Planetary Institute, Houston, TX. <https://www.hou.usra.edu/meetings/lpsc2018/pdf/1474.pdf>
- Pasckert, J. H., Hiesinger, H., & van der Bogert, C. H. (2018). Lunar farside volcanism in and around the South Pole–Aitken basin. *Icarus*, 299, 538–562. <https://doi.org/10.1016/j.icarus.2017.07.023>
- Pike, R. J. (1974). Ejecta from large craters on the Moon: Comments on the geometric model of McGetchin et al. *Earth and Planetary Science Letters*, 23(3), 265–271. <https://doi.org/10.1016/0012-821X>
- Potter, R. W. K., Kring, D. A., Collins, G. S., Kiefer, W. S., & McGovern, P. J. (2013). Numerical modeling of the formation and structure of the Orientale impact basin. *Journal of Geophysical Research: Planets*, 118, 963–979. <https://doi.org/10.1002/jgre.20080>
- Qiao, L., Ling, Z., Fu, X., & Li, B. (2019). Geological characterization of the Chang'e-4 landing area on the lunar farside. *Icarus*, 333, 37–51.
- Robinson, M. S., Brylow, S. M., Tschimmel, M., Humm, D., Lawrence, S. J., Thomas, P. C., et al. (2010). Lunar Reconnaissance Orbiter Camera (LROC) instrument overview. *Space Science Reviews*, 150, 81–124.
- Schultz, P., & Gault, D. E. (1985). Clustered impacts: Experiments and implications. *Journal of Geophysical Research*, 90(B5), 3701–3732. <https://doi.org/10.1029/JB090iB05p03701>
- Smith, D. E., Zuber, M. T., Jackson, G. B., Cavanaugh, J. F., Neumann, G. A., et al. (2010). The Lunar Orbiter Laser Altimeter investigation on the Lunar Reconnaissance Orbiter Mission. *Space Science Reviews*, 150, 209–241.
- Wang, Y., Xie, M., Xiao, Z., & Cui, J. (2020). The minimum confidence limit for diameters in crater counts. *Icarus*, 341, 113645. <https://doi.org/10.1016/j.icarus.2020.113645>
- Whitten, J., Head, J. W., Staid, M., Pieters, C. M., Mustard, J., Clark, R., et al. (2011). Lunar mare deposits associated with the Orientale impact basin: New insights into mineralogy, history, mode of emplacement, and relation to Orientale Basin evolution from Moon Mineralogy Mapper (M3) data from Chandrayaan-1. *Journal of Geophysical Research: Planets*, 116, E00G09. <https://doi.org/10.1029/2010JE003736>
- Wu, W., Li, C., Zuo, W., Zhang, H., Liu, J., Wen, W., et al. (2019). Lunar farside to be explored by Chang'e-4. *Nature Geoscience*, 12(4), 222–223. <https://doi.org/10.1038/s41561-019-0341-7>
- Xiao, Z. (2016). Size-frequency distribution of different secondary crater populations: 1. Equilibrium caused by secondary impacts. *Journal of Geophysical Research: Planets*, 121, 2404–2425. <https://doi.org/10.1002/2016JE005139>
- Xiao, Z. (2018). On the importance of self-secondaries. *Geoscience Letters*, 5, 17.
- Xie, M., Liu, T., & Xu, A. (2020). Ballistic sedimentation of impact crater ejecta: Implications for the provenance of lunar samples and the resurfacing effect of ejecta on the lunar surface. *Journal of Geophysical Research: Planets*, 125, e2019JE006113. <https://doi.org/10.1029/2019JE006113>
- Xie, M., Xiao, Z., Zhang, X., & Xu, A. (2020). The provenance of regolith at the Chang'e-5 candidate landing region. *Journal of Geophysical Research: Planets*, 125, e2019JE006112. <https://doi.org/10.1029/2019JE006112>
- Yingst, R., Chuang, F., Berman, D., & Mest, S. (2017). *Geologic Mapping of the Planck Quadrangle of the Moon (LQ-29)*. Paper presented at the 48th Lunar and Planetary Science Conference, Lunar and Planetary Institute, Houston, TX. <https://www.hou.usra.edu/meetings/lpsc2017/pdf/1680.pdf>
- Zhang, L., Li, J., Zeng, Z., Xu, Y., Liu, C., & Chen, S. (2020). Stratigraphy of the Von Kármán Crater Based on Chang'E-4 Lunar Penetrating Radar Data. *Geophysical Research Letters*, 47, e2020GL088680. <https://doi.org/10.1029/2020GL088680>

## Reference from the Supporting Information

- Knight, R. J., Irving, J. D., Tercier, P., Freeman, G. J., Murray, C. J., & Rockhold, M. L. (2007). A comparison of the use of radar images and neutron probe data to determine the horizontal correlation length of water content. In D. W. Hyndman, F. D. Day-Lewis, & K. Singha (Eds.), *Subsurface hydrology: Data integration for properties and processes* (pp. 171). Wiley.
- Sandmeier, K. J. (2010). Non-destructive testing of concrete with electromagnetic and acoustic–elastic waves: data analysis. In C. Maihofer, H. Reinhardt, & G. Dobmann (Eds.), *Non-destructive evaluation of reinforced concrete structures* (pp. 125–143). Woodhead Publishing.
- Schneider, W. A. (1978). Integral formulation for migration in two and three dimensions. *Geophysics*, 43(1), 49–76.